Chapter 5

Investigation of Multifaceted Properties for Environment friendly

$(1\text{-}x)LiNbO_3\text{-}x(Li_{0.5}Dy_{0.5})TiO_3$

Solid Solution

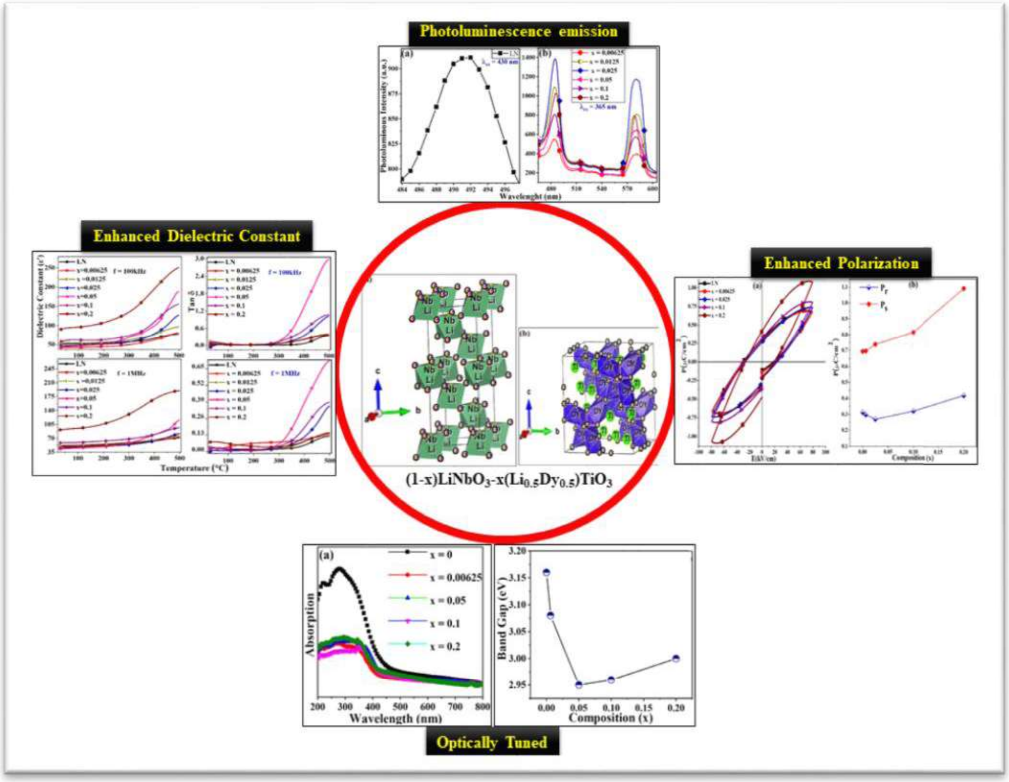

Chapter 5. Investigation of Multifaceted Properties for Environment friendly(1-x)$LiNbO_3$-x($Li_{0.5}Dy_{0.5}$)TiO_3 Solid Solution

5.1 Introduction

As we have discussed earlier in Chapter 1, numerous research works have been reported on LN-based ceramics for different kinds of applications. Chapter 3 and chapter 4 are based on additive addition and single rare earth doped, respectively, in $LiNbO_3$. The two element co-doping in $LiNbO_3$ is rarely reported for the investigation of the LN ceramic for the electrical and optical properties. The co-doped LN solid solution ceramic might be an emerging material for a wide range of applications. The co-doping combination of Low electrical conductivity-based material and good phosphorous property-based material that is also thermally very stable at high temperatures can make the LN ceramic more worthy for Electrical energy applications and optical properties-based applications at high temperatures by maintaining the curie temperature very high. Co-doping in LN can change the structural properties, which can bring some changes that can turn LN into a high-potential ceramic material for optical and electrical energy-based sensing devices and optical display applications. High curie temperature is the most attractive key factor of LN, so much research related to high-temperature applications has been published. Such low-cost synthesized and high-potential materials can contribute to new technological advancement in respective areas. Here, we are discussing some recent literature related to Co-doped LN solid solution ceramics, which can put up the related information about related work, which we are going to discuss in this chapter, and the literature survey is as follows.

L.X. Lovisa it has published an article on the investigation of structural, morphological, and photoluminescent properties for non-stoichiometric $LiNbO_3$

Nanoparticles for co-doped rare earth materials Dy^{3+}/Tb^{3+}. Through their XRD investigation, the secondary phase of Li_3NbO_4 has been confirmed in their synthesized materials because of the non-stoichiometry of $LiNbO_3$. Their findings indicate that the presence of photoluminescence properties is associated with surface defects in the particles, which also facilitate the recombination of photo-generated charges that are favorable to photoluminescence properties. The minimum band gaps for LN:1% Dy, LN:1% Tb, and pure LN are 4.17 eV, 4.25 eV, and 4.21 eV, respectively, while two band gaps of 3.63 eV and 3.59 eV are observed for the 1%Dy and 1%Tb co-doping with LN [1]. Saito et al. reported the synthesis of a $(K_{0.44}Na_{0.52}Li_{0.04})(Nb_{0.86}Ta_{0.10}Sb_{0.04})O_3$ ceramic characterized by a pronounced [001] texture. This ceramic exhibits a polymorphic phase transition (PPT) occurring between ferroelectric orthorhombic and tetragonal phases in the vicinity of room temperature. This material exhibited good performance equal to that of the PZT family [2]. The piezoelectric and dielectric properties of the system $K_{0.95}Li_{0.05}Ta_{1-x}Nb_xO_3$ (KLTN, $x = 0.51$, 0.60, 0.69 and 0.78), were examined by Jun Li et al., Using pyroelectric and dielectric measurement, they were able to determine the Curie temperature as well as the phase change. The piezoelectric properties were exceptionally appealing at a composition of $x = 0.60$, and a saturated PE hysteresis loop was also obtained [3].

The objectives of the present work are (i) to synthesize $(1-x)LiNbO_3-x(Li_{0.5}Dy_{0.5})TiO_3$ ceramic materials for the various composition $x = 0.0$, 0.00625, 0.0125, 0.025, 0.05, 0.1 and 0.2, via solid-state reaction method at low cost and investigate the effect of Dy^{3+} and Ti^{4+} co-doping in $LiNbO_3$ on the crystal structure and microstructure, (ii) to investigate the dielectric characteristics in a wide range of frequencies with varying temperature (iii) to investigate and analyze ferroelectric characteristic at room temperature as well as calculate the energy density for the prepared materials (iv) to investigate the optical and photoluminescence properties of prepared samples.

5.2 Experimental

The lead-free (1-x)$LiNbO_3$-x($Li_{0.5}Dy_{0.5}$)TiO_3 solid solutions were synthesized using high-temperature ceramic synthesis. Stoichiometric amounts of Nb_2O_5 (Sigma Aldrich, 99.99%), Dy_2O_3 (Sigma Aldrich, 99.99%), TiO_2 (Himedia, 99%), and Li_2CO_3 (Himedia, 98.5%) were milled in an ethanol-wet medium in a high-energy planetary ball mill for 12 hours at the speed of 300 rpm. After completion of the milling process, the milled wet solid solution was collected and kept on a hot plate at 100°C to dry the wet sample. Then, the dried solution was calcined at 800°C for 6 hrs with a heating rate of 3 °C/minute. After that, the calcined powder was mixed with a binder of polyvinyl alcohol (PVA) and converted into a disc of 10 mm diameter at a uniaxial pressure of 5 tons. The green pellet was fired at 550°C for 8 hours to eliminate the binder, and then it was sintered at a temperature of 1050°C for 6 hrs. Sintering was performed in a closed environment for that sealing of magnesium oxide used due to its non-reactive nature and very high thermal stability [4]. Then, the sintered pellet was crushed into fine powder and annealed at 500°C for 12 hours.

X-ray diffraction (XRD) of annealed solid solutions was recorded in the 2θ range from 20º to 80º at a scan rate of 2°/minute using a Miniflex600 X-Ray diffractometer having CuKα radiation (1.5406 Å) provided by Rigaku, Japan. The crystallographic phase was validated with the help of the X-pert high score software as well as the ICDD database. The FullProf Suite software was employed to refine the structural parameters through the Rietveld refinement method[5,6]. The VESTA (Visualization for Electronic Structural Analysis) software was used to draw the three-dimensional crystal structure.

An X-ray photoelectron spectroscopy (XPS) characterization was carried out using the K_α X-ray Photoelectron Spectrometer system. For the excitation, an Al K_α monochromatic X-ray source with an energy of 1486.6 eV was used, and the test depth was kept at 10 nm while the temperature was kept at room temperature. This has been done in order to determine the elemental composition of the material that has been prepared, in addition to the chemical and atomic states that are present in the materials. The morphological microscopic investigation was carried out at room temperature using scanning electron microscopy (JCM-6000 Plus BenchTop Sem Neoscope, JEOL Asia PTE Ltd), and ImageJ software was utilized to determine the average grain size of the sintered pellets. The dielectric properties were examined by employing an impedance spectroscopic analyzer (Keysight E4990A Impedance analyzer) at frequencies 1 kHz, 100 kHz and 1 MHz and the temperatures ranging from room temperature to 500 °C. The results of these evaluations can be found in the table below. At room temperature, ferroelectric properties were analyzed using a ferroelectric tester of Radiant Technology (Precision Premier-II). Nicolet Summit FTIR Spectrometers were utilized in order to carry out the FTIR analysis of the functional group as well as the purity of the sample that was prepared. The absorbance properties of the prepared system were characterized through JASCO V-650 UV-visible spectrophotometer with a spectral range of 200-800 nm and a scan rate of 2 nm/s at room temperature and also the direct band gap was calculated through Tauc Plot equation. The fluorescence spectrometer, namely the Hitachi F-4600 model, was used to determine the excitation and emission spectra of the annealed powder from the prepared samples. The measurements were conducted within the wavelength range of 350–700 nm.

5.3 Results and discussion

5.3.1 Crystal structure analysis

The **Figure 5.1** displays the powder XRD patterns of annealed (1-x)$LiNbO_3$-x$(Li_{0.5}Dy_{0.5})TiO_3$ (LNDT) ceramics for various compositions with x = 0.0, 0.00625, 0.0125, 0.025, 0.05, 0.1 and 0.2. The diffraction peaks of each sample have been indexed using the standard XRD pattern of $LiNbO_3$ (JCPDS File #98-001-631) having space group R3c and values of corresponding (hkl) are shown in the **Figure 5.1**. Further, there are three very small peaks at 28.37°, 30.00° and 49.88° arising in all doped compositions and some others additional peaks are observed in the composition x = 0.2. These additional peaks, marked with plus (+) sign; appear due to partial reaction of dysprosium and titanium with host matrix LN. Since, the ionic radii of Li^+ is 0.92 Å [7], whereas the ionic radii of Dy^{3+} is 1.253 Å[8]. The ionic size of Dy^{3+} ion as compare to Li^+ ion creates disturbance in the grain orientation of c-axis. It has been found that the additional peaks are attributed to a secondary phase of Dy_2TiO_5 (JCPDS #98-001-5676) having space group $F\bar{4}3m$, as confirmed from the X-pert high score plus software.

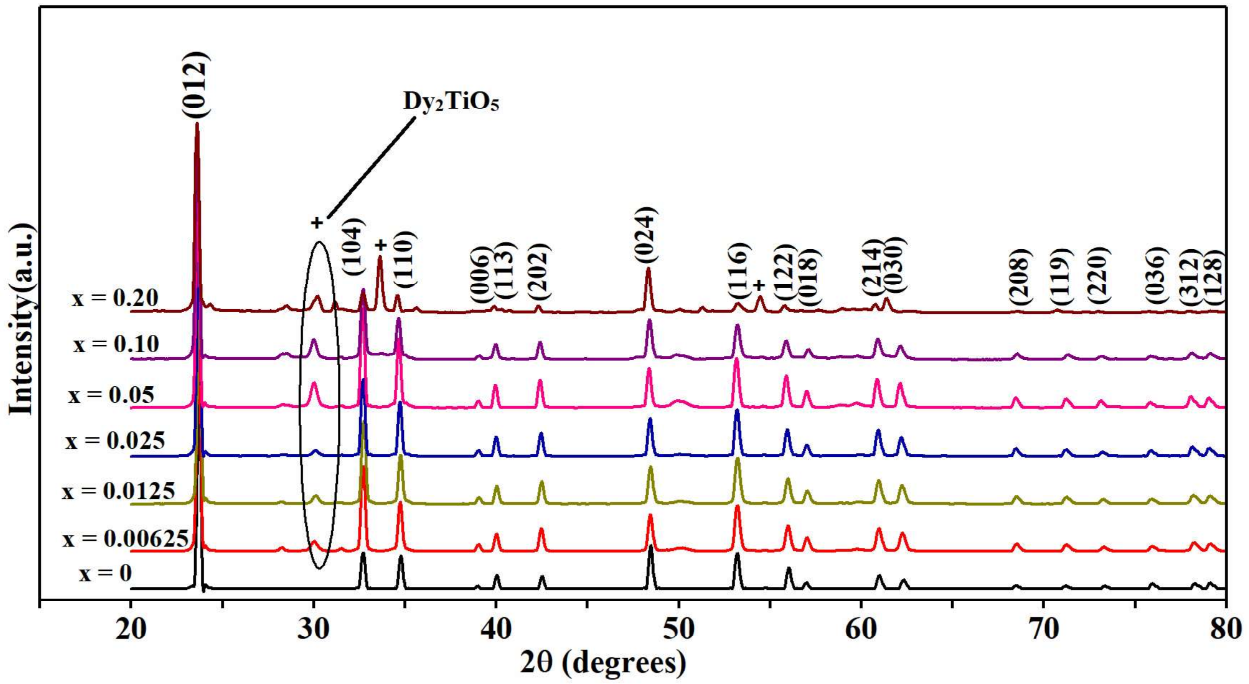

Figure 5.1: XRD Pattern of (1-x)LiNbO$_3$-x(Li$_{0.5}$Dy$_{0.5}$)TiO$_3$ ceramic for different composition (x)

For the estimation of lattice parameters and unit cell volume, Rietveld structure refinement has been performed. Rietveld structure refinement has been carried out for all compositions using R3c and F$\bar{4}$3m space groups. A very refined Rietveld fit has been obtained for all the compositions. Rietveld structure refinement confirms that (1-x)LiNbO$_3$-x(Li$_{0.5}$Dy$_{0.5}$)TiO$_3$ ceramics for $x \neq 0$, crystallize into cubic crystal structure with F$\bar{4}$3m space group and rhombohedral crystal structure with R3c space group. However, the pure LiNbO$_3$ ceramic crystallizes into a single phase of rhombohedral crystal structure with R3c space group. Rietveld fits for LiNbO$_3$ and (1-x)LiNbO$_3$-x(Li$_{0.5}$Dy$_{0.5}$)TiO$_3$ with x = 0.1 are shown in the **Figure 5.2**. The obtained values of lattice parameters and unit cell volume for rhombohedral and cubic crystal structures have been listed in **Table 5.1** and **Table 5.2**, respectively. A slight modification in the lattice parameters and unit cell volume has been observed due to presence of different ions with different ionic radii. The elements dysprosium and titanium partially react with the $LiNbO_3$ matrix, which led to an irregular modification in unit cell volume as well as lattice parameters.

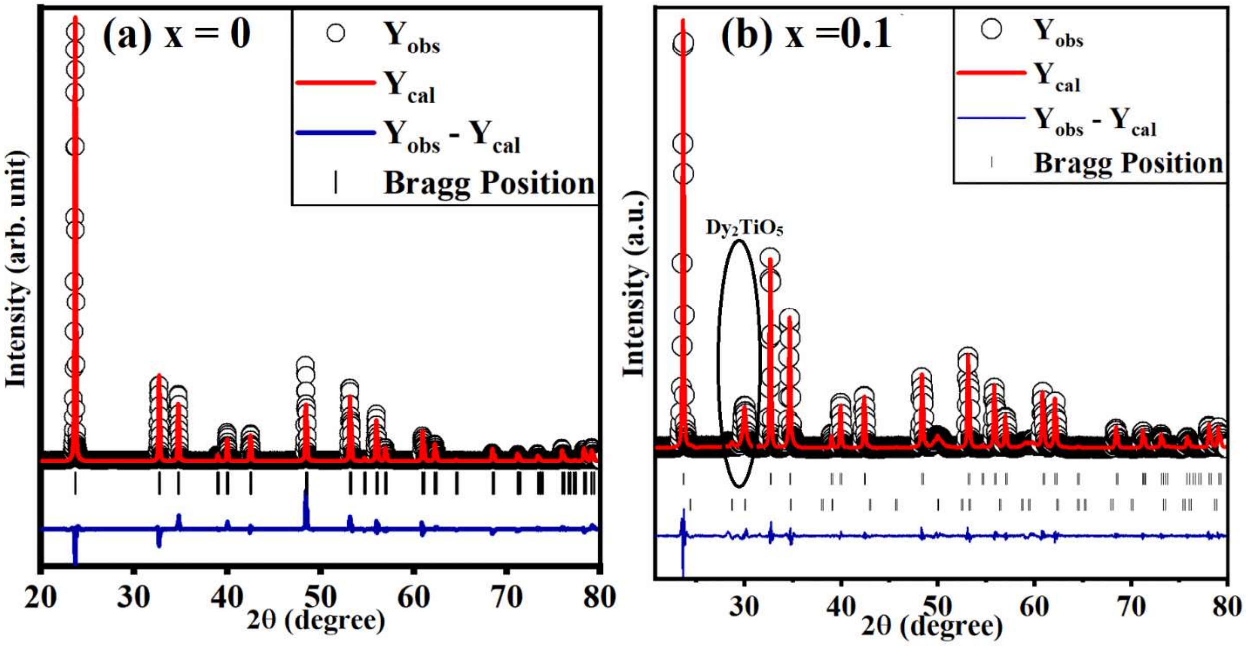

Figure 5.2(a-b) : Rietveld structure refined fits for (a) $LiNbO_3$ and (b) $(1-x)LiNbO_3-x(Li_{0.5}Dy_{0.5})TiO_3$ where x = 0.1.

Table 5.1: Lattice parameters and unit cell volume of primary phase $(1-x)LiNbO_3-x(Li_{0.5}Dy_{0.5})O_3$ of samples

Composition	a (Å)	b (Å)	c (Å)	V (Å^3)
x = 0.00	5.1631(1)	5.1631(1)	13.8703(3)	320.23(1)
x = 0.00625	5.1645(1)	5.1645(1)	13.8498(5)	319.92(2)
x = 0.0125	5.1635(1)	5.1635(1)	13.8395(6)	319.56(2)
x = 0.025	5.1674(1)	5.1674(1)	13.8508(4)	320.30(1)
x = 0.05	5.1742(1)	5.1747(1)	13.8519(3)	321.17(1)
x = 0.1	5.1711(3)	5.1711(3)	13.8192(1)	320.03(3)

Table 5.2: Lattice parameters and unit cell volume of secondary phase of (1-x)$LiNbO_3$-x$(Li_{0.5}Dy_{0.5})O_3$ samples

Composition	a = b = c (Å)	V (Å^3)
x = 0.00625	10.3182(1)	1098.56(1)
x = 0.0125	10.2847(8)	1087.88(1)
x = 0.025	10.2879(3)	1088.55(5)
x = 0.05	10.3181(7)	1098.52(4)
x = 0.1	10.3179(4)	1098.44(7)

Ball and stick molecular models have been drawn using VESTA software. The **Figure 5.3(a)** shows ball and stick molecular unit cell models for rhombohedral crystal structure having R3c space group. However, the **Figure 5.3(b)** displays ball and stick molecular unit cell model for cubic crystal structure having F$\bar{4}$3m space group.

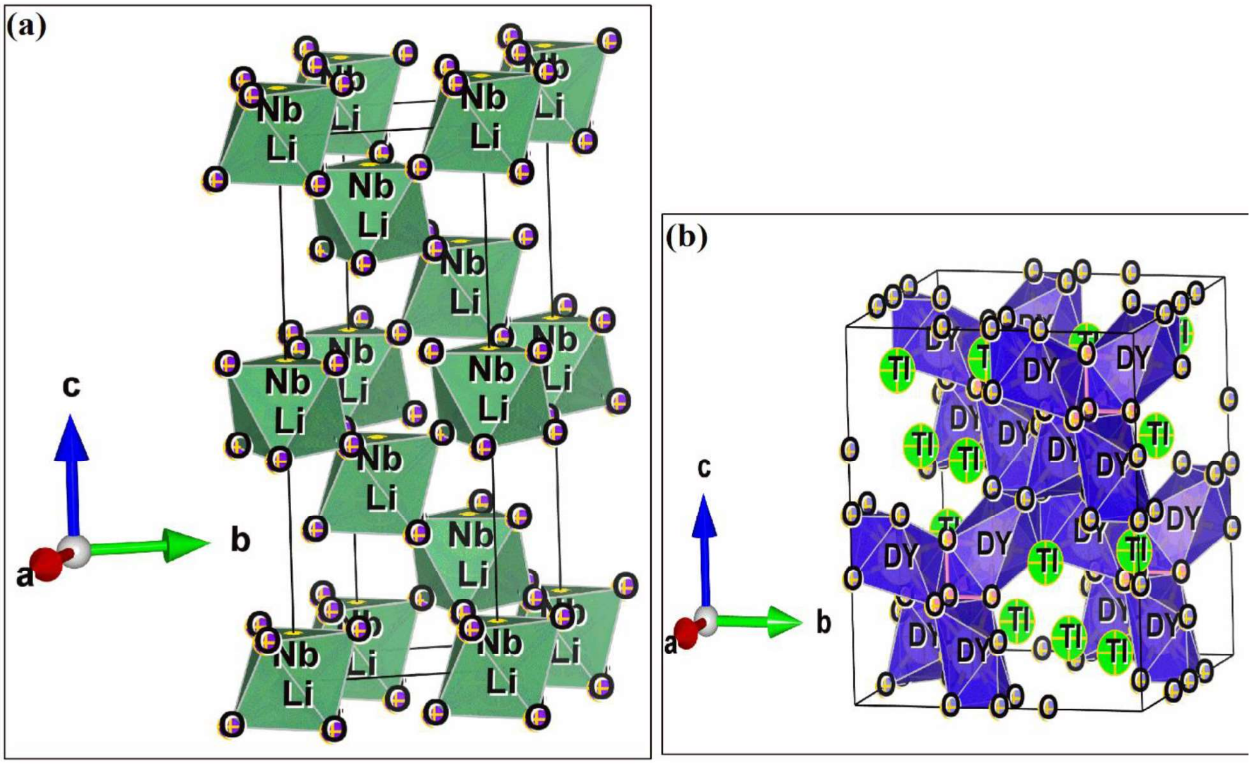

Figure 5.3: Crystal structure of (1-x)$LiNbO_3$-x$(Li_{0.5}Dy_{0.5})O_3$ with mix phases; (a) Rhombohedral phase and (b) cubic phase.

5.3.2 Morphological analysis

The **Figure 5.4(a-f)** shows the surface morphology of highly compact pellets of pure LN and solid solutions of Lithium niobate dysprosium titanate based solid solution materials. In the case of pure LN the **Figure 5.4(a)**, The synthesized pure lithium niobate crystalline exhibits regular grain formation and also showcasing a distinct and well-defined rhombohedral crystal shape[9]. Furthermore, the grain morphology exhibits clarity and distinctiveness, featuring well-defined grain boundaries. The average grain size, approximately 3.46 μm, was determined through calculations using ImageJ software[10,11]. The average grain size of $(1-x)LiNbO_3-x(Li_{0.5}Dy_{0.5})TiO_3$ based solid solution compound is found between 1.09 to 1.85 μm for the composition varies from $x = 0.00625$ to $x = 0.2$. In our study up to $x = 0.1$ there are not very abruptly changes in grain formation but it can be seen very plainly that the morphology of the prepared solid solution completely changes when the composition is changed to $x = 0.2$. It would appear that the shape of grains changes from that of regular rhombohedral crystals shape to that of plates like shape as a result of the formation of super structures when the percentage of Ti ion in the system is increased which is shown in the **Figure 5.4(g)**. H. Nakano et al. reported that changes to the c-axis lattice constant occurred in $Li_{1+x-y}M_{1-x-3y}Ti_{x+4y}O_3$ ($M = Nb^{5+}$, Ta^{5+}) after a superstructure with an increased Ti ion concentration was formed. Throughout this process, the size of the c-axis cells decreased with time until they reached a certain point, which indicated the beginning of a restricted period. On the other hand, as the Ti ion content in the prepared system increased, the a-axis cell size stayed basically the same [12,13].

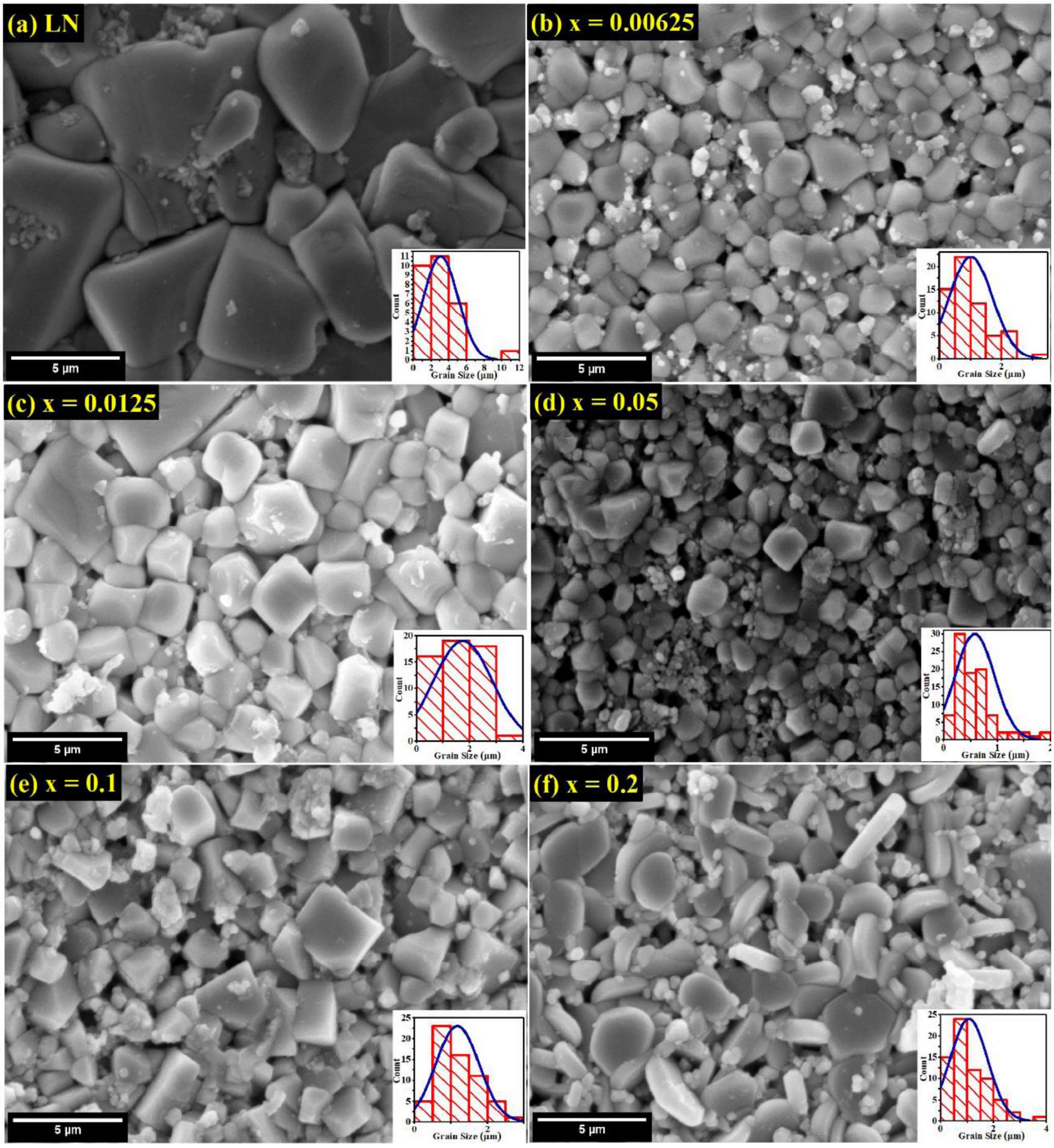

Figure 5.4: (a-g) Scanning electron microscopic images of (1-x)$LiNbO_3$ -x($Li_{0.5}Dy_{0.5}$)TiO_3, where (a) x = 0, (b) x = 0.00625, (c) x = 0.0125, (d) x = 0.05, (e) x = 0.1, (f) x = 0.2.

5.3.3 Thermogravimetric analysis

The **Figure 5.5** demonstrate the Thermogravimetric (TGA) response of lithium niobate ($LiNbO_3$) and its composition variations with lithium dysprosium titanate ($Li_{0.5}Dy_{0.5}TiO_3$), across a temperature range from 35°C to 900°C. The TGA curve for pure $LiNbO_3$ exhibits a monotonous weight loss, which stabilizes near 900°C, suggesting a total mass reduction of approximately 2.5%. This trend is indicative of decomposition processes, potentially encompassing lithium volatility, material breakdown, or moisture evaporation. For the solid solution samples, the weight loss is confined to a narrower temperature window (270°C to 440°C), with a net diminution of around 1.1%. Beyond this range, the curves exhibit a modest reversal, with the sample mass incrementing slightly, an anomaly that can be ascribed to the material's interaction with atmospheric oxygen—a hallmark of oxidation at high temperatures. This inflection point, denoting a transition from weight loss to gain, necessitates a rigorous examination of the sample environment and experimental setup. The observed weight increase may also be influenced by phenomena such as the buoyancy effect, absorption, adsorption, or nitride formation under specific gaseous conditions. The buoyancy phenomenon arises from the decrease in density of the surrounding gas when subjected to heating [14–17]. A noticeable increase in weight ranging from 50 μg to 200 μg is usually the outcome of this. Each of these factors underscores the material's reactive nature under thermal duress and should be meticulously accounted for when postulating on the material's thermal stability and its adaptability to high-temperature applications.

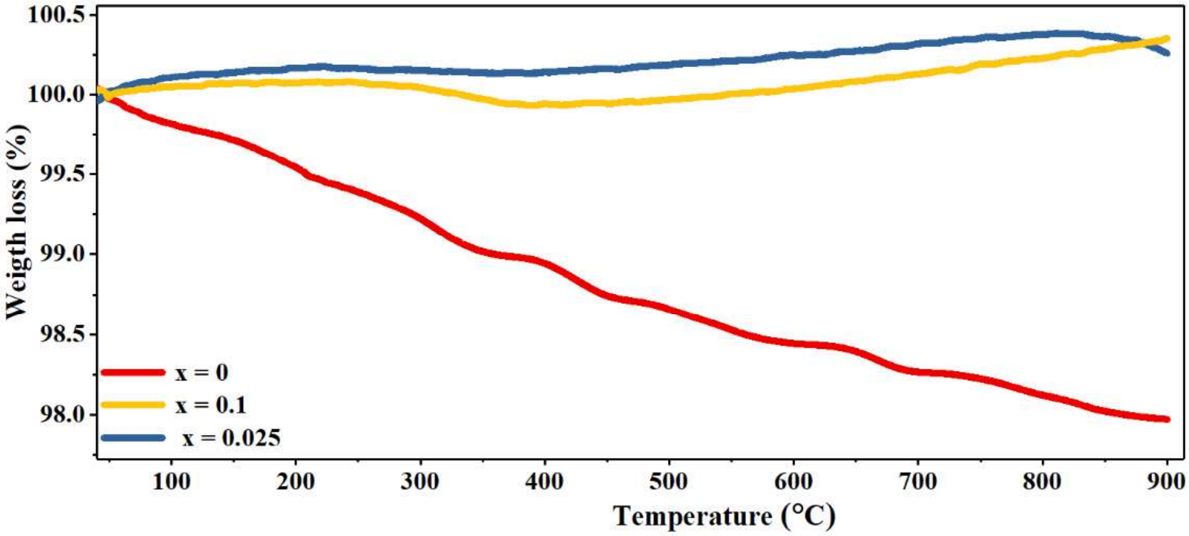

Figure 5.5: Thermogravetric analysis of Pure Lithium Niobate and (1-x)$LiNbO_3$-x$Li_{0.5}Dy_{0.5}TiO_3$ for x = 0.1

5.3.4 X-ray Photoelectron Spectroscopy Study

Figure 5.6 (a-e) are illustrated the X-ray photoelectron spectroscopy spectrum of lithium niobate disprosium titanate solid solution for the detailed chemical and eletronic state investigation. The calibration was performed utilising the C1s binding energy of carbon contamination in order to adjust for charging effects. This value was determined to be 284.5 eV after being measured. After applying the Shirley-type background subtraction, the results were as follows:

XPS spectra of O1s shown in the **Figure 5.6(a)** is as similar as previous reported[18,19].3435 Using the Lorentzian-Gaussian distribution function, the spectrum of O1s may be divided into two peaks. The narrow and high intensity peak is obseved at lower Binding Enrgy (B.E.) 529.12 eV which is belongs to the lattice oxygen of $LiNbO_3$ and is obvious to be attributed to O^{2-} ions and the broad and low intensity peak obsreved at higher B.E. 531.46 eV is associated with oxygen ions in the oxygen vacancy region and it is corresponds to O^{1-} ions[20,21]. As seen in the **Figure 5.6 (b)** it shows the Li1s and Nb4s XPS spectrum at B.E. 54.15 eV and 59.39 eV is similar to previously reoported researchers[19,22].

Its indicating that Lithium is remains present in standard state Li^+. The Nb4s peak can be found in the spectrum at 59.39 eV, and it is possible that this peak was caused by the Nb ions that were present in the LNDT system. There is a possibility that the bonding in Li-Nb-O is directly related to the Nb4s peak[23,24]**.** In the **Figure 5.6 (c)** The peaks of Nb3d that were found to be located at 206.08 eV and 208.8 eV were assigned to the spin states of Nb $3d_{5/2}$ and Nb $3d_{3/2}$, respectively.This indicates that Niobium is present in the chemical state of Nb^{5+}, a finding consistent with earlier research [25,26]. In the Fig. 6(d) XPS Spectra of Dy3d shown with two peaks at 1303.56 eV and 1295.03 eV and thsese two peaks are attributed to the spin states of Nb $3d_{3/2}$ and Nb $3d_{5/2}$, respectively, and is is found that Dysprosium exist with Dy^{3+} state which is similar to previous reported research[27,28]**.** The XPS spectra of Ti $2p_{3/2}$ and Ti $2p_{1/2}$ are shown in the **Figure 5.6 (e)** at 457.63 eV and 462.57, 463.65 eV, respectively. These values are consistent with the findings of other reports regarding the structure of TiO_6 octahedrons. Ti^{4+} signals are strongly detected but weaker spectra of Ti^{3+} signals also detected which may be due to that the presence of Nb^{5+} reduced the part of Ti^{4+} to Ti^{3+} as previously reported research[29,30].

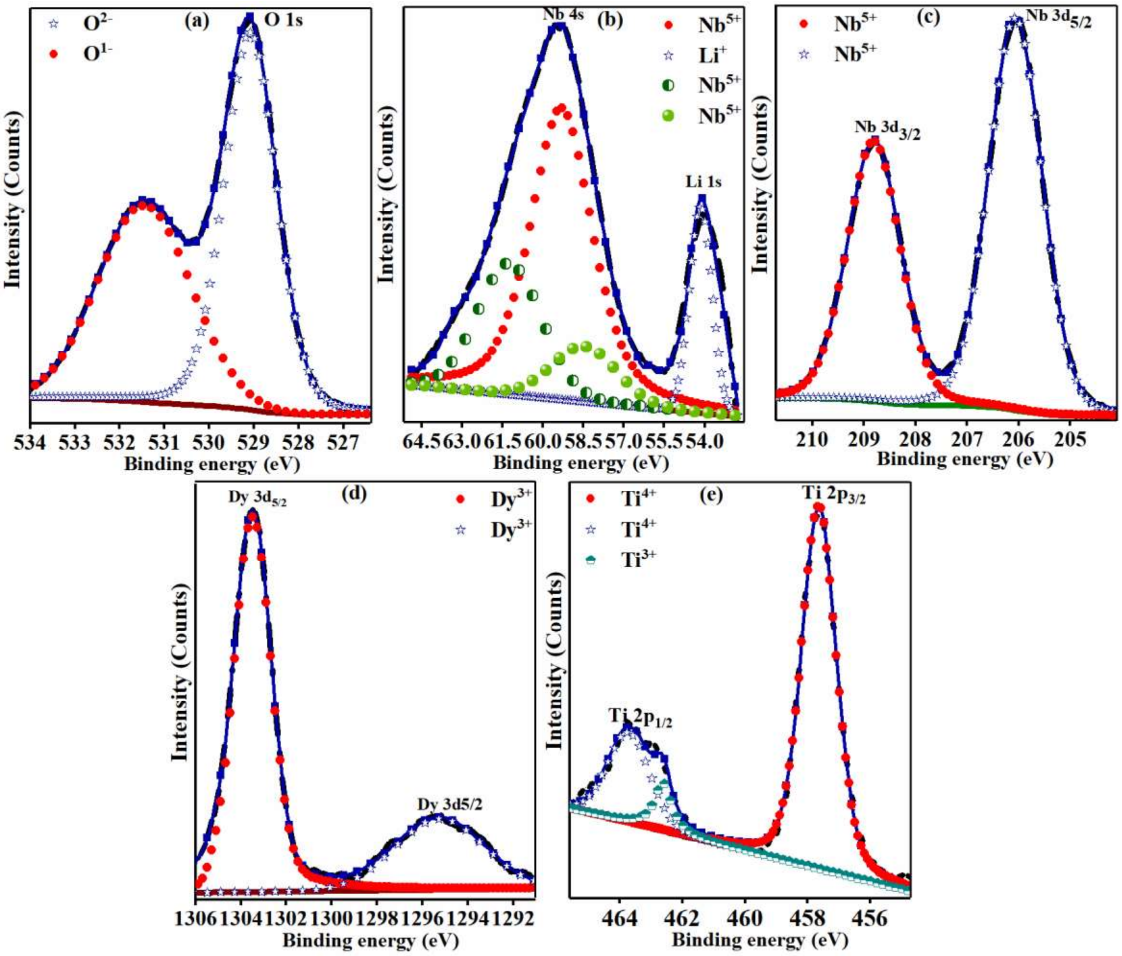

Figure 5.6(a-e): X-ray photo electron spectra of (1-x)$LiNbO_3$-x$(Li_{0.5}Dy_{0.5})TiO_3$ for x = 0.1, (a) Fitting of Nb 4s, Li 1s spectra, (b) Fitting of O1s spectra (c) Fitting of Nb 3d spectra, (d) Fitting of Dy 3d spectra, (e) Fitting of Ti 2p spectra,

5.3.5 Fourier transform infrared spectroscopy spectra (FTIR) analysis

The FTIR investigation has been carried out in order to provide information about the quality and consistency of the samples that have been synthesized, and the results of this investigation are displayed in the **Figure 5.7**, the FTIR spectra of pure LN and (1-x)$LiNbO_3$-x$(Li_{0.5}Dy_{0.5})TiO_3$ solid solution for the different x values. The absorption band(s) observed at 3440, 2922, 1640, 1142, 943, 643, and 469 cm^{-1}. The absorption band at 3440 and 2922 cm^{-1} in the FTIR spectra is due to the OH vibration in an oxygen plane which is perpendicular to the c-axis. The bands that were observed are associated with the OH molecular defect that is located in the oxygen plane. Each of the multiple peaks in these bands corresponds to a unique location of the proton (H^+) in the oxygen plane. These bands are able to be resolved more clearly as the crystal moves closer to its stoichiometric composition. The identified OH peaks are ascribed to metal hydroxide bonds, which are hypothesized to have formed as a result of moisture entrapment during crystal growth[31,32], these OH vibrations are also indication of that sample contains any organic compound despite the fact that the XRD measurements gave no indication of anything**,** The existence of a broad peak at 1142 cm^{-1} may be ascribed to the residual CO_3^{2-} ions contained within the crystalline matrix, which signifies that the decomposition of the Li_2CO_3 remains incomplete[31]. These bands are the distinguishing characteristics of the LN IR fingerprint absorption. It has been determined that the Nb-O vibration in the crystalline state LN is responsible for the absorption band in the range 679 to 681 cm^{-1}[33,34]. The single bond between Li and O detected at wavelength 943 cm^{-1} and the nano crystallinity of the synthesized sample is confirms through a peak observed at 469 cm^{-1}.

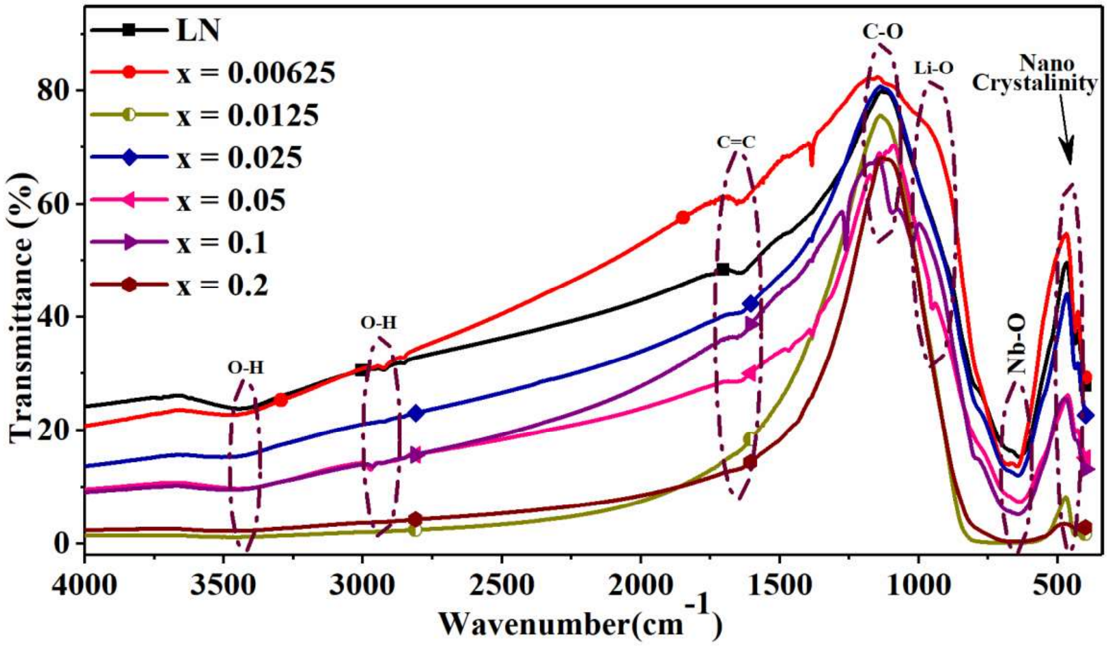

Figure 5.7: Fourier transform infrared spectroscopy spectra of (1-x)$LiNbO_3$-x($Li_{0.5}Dy_{0.5}$)TiO_3 for different value of x at room temperature.

5.3.6 UV-Vis Spectroscopy Analysis

The optical properties of all solid solutions were studied by collecting the absorption spectra. Optical absorption spectra, as shown in the **Figure 5.8**(a), provide evidence for the effect of $Li_{0.5}Dy_{0.5}TiO_3$ doping percentage on the optical band gap of (1-x)$LiNbO_3$-x$(Li_{0.5}Dy_{0.5})TiO_3$ solid solution for various compositions. For (1-x)$LiNbO_3$-x$(Li_{0.5}Dy_{0.5})TiO_3$ solid solution, the indirect band gap was calculated using well-known Tauc equation $(\alpha h\upsilon)^{0.5}$ vs hυ where hυ is band gap energy, α is absorption coefficient and B is referred as Tauc constant [35]. As depicted in the **Figure 5.8**(b), Un-doped $LiNbO_3$ shows much lower value of indirect band gap (E_g = 2.4 eV) as earlier reported value (E_g = 3.3 eV) in literature [36]**.** After raising the x($Li_{0.5}Dy_{0.5}TiO_3$) contents in (1-x)($LiNbO_3$) further, the indirect band gap increases but there is no confirmed tangent line observed, so, we have also calculated the direct band gap. The direct band gap of (1-x)$LiNbO_3$-x$(Li_{0.5}Dy_{0.5})TiO_3$ samples were determined using the Tauc's equation $\alpha h\nu = B(h\nu - E_g)^2$. A tangent line is drawn on $(\alpha h\nu)^2$ vs hν plot to get the band gap value as shown in the **Figure 5.8**(c) [37]**.** After raising the x($Li_{0.5}Dy_{0.5}TiO_3$) contents in (1-x)$LiNbO_3$ further, the direct band gap decreases to 3.08 eV for composition x = 0.00625 and then further decreased for composition x = 0.05. Further doping (x = 0.2) cause slight increase in band gap values as shown in the **Figure 5.8**(d). For the composition x= 0.05, absorption is higher in visible range which is may be due to coupling between Dy ion and oxygen vacancies [38]. This composition also exhibits the lowest band gap (2.95 ± 0.003 eV) which can be attributed to the creation of sub-bands between the conduction band and valence band as a result of Ti and Dy doping and the existence of oxygen vacancies. The CBM tail is extended and the band gap is lowered as a result of the sub-bands created by Ti and Dy doping and oxygen vacancies [39].

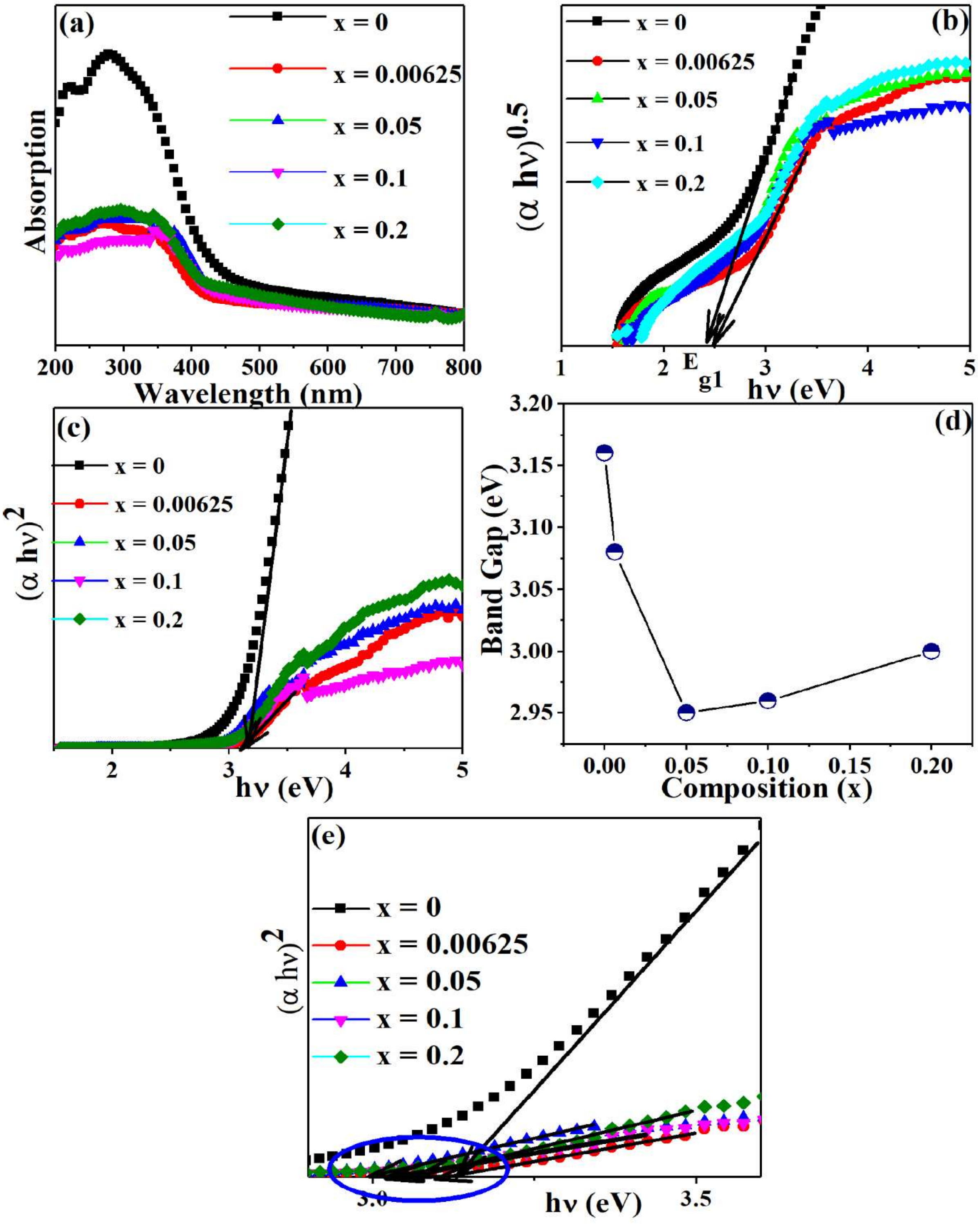

Figure 5.8(a-e): (a) Variation of absorption spectra of (1-x)$LiNbO_3$-x$(Li_{0.5}Dy_{0.5})TiO_3$ solid solutions for various compositions in the range ($0.0 \leq x \leq 0.2$). (b) Indirect band gap of (1-x)$LiNbO_3$-x$(Li_{0.5}Dy_{0.5})TiO_3$ solid solutions (c) Direct band gap of (1-x)$LiNbO_3$-x$(Li_{0.5}Dy_{0.5})TiO_3$ (d) Direct band gaps for (1-x)$LiNbO_3$-x$(Li_{0.5}Dy_{0.5})TiO_3$ solid solution with composition variation, (e) Direct band gap showing exact tangential point.

5.3.7 Photoluminescence Spectroscopy Analysis

We have investigated the composition dependent photoluminescence (PL) emission at room temperature for (1-x)$LiNbO_3$-x($Li_{0.5}Dy_{0.5}TiO_3$) solid solutions. The PL emission studies of $LiNbO_3$ and $Li_{0.5}Dy_{0.5}TiO_3$ doped $LiNbO_3$ solid solutions in the range of 430-600 nm wavelengths are carried out. $LiNbO_3$ is doped with rare earth element Dy as Dy^{3+} ion has long energy level life. Doping with Dy^{3+} ion make this ceramic useful for yellow lasers[40]. In $LiNbO_3$, Li^+ ions are less number than that of Nb^{5+} and this causes optical damage [41]. So, extra Li doping in $LiNbO_3$ will reduce the optical damage[41,42]. The $LiNbO_3$ sample is excited at 430 nm. $LiNbO_3$ exhibits PL emission in UV-visible light region and shows cyan colour emission at 485-500 nm as shown in the **Figure 5.9(a)**. This broad emission peak of cyan colour luminescence was detected in all samples. $Li_{0.5}Dy_{0.5}TiO_3$ doped $LiNbO_3$ solid solutions showed two broad PL emission peaks in UV-visible light region 470-497 nm and 560-596 nm as shown in the **Figure 5.9(b)**. The first broad peak in the range 470-497 nm deconvoluted and it is found that it combined both blue and cyan colours spectrum as shown in the **Figure 5.10(b)**. So, (1-x)$LiNbO_3$-x($Li_{0.5}Dy_{0.5}TiO_3$) solid solutions show blue, cyan and yellow emission peaks. The undoped $LiNbO_3$ doesn't emit the blue colour emission as confirmed after peak fitting shown in the **Figure 5.10(a)**. The blue peak at 477 nm in (1-x)$LiNbO_3$-x($Li_{0.5}Dy_{0.5}TiO_3$) compositions generated due to defect energy levels. These defect energy levels formed due to doping of Dy and Ti. Cyan emission peak is more dominant around 483-500 nm. The observed blue and cyan emission peaks are due to presence of oxygen vacancies [43]**.** When $LiNbO_3$ doped with Dy and Ti, it creates oxygen vacancies. These oxygen vacancies form new sub band energy levels. Fully ionized oxygen vacancies give rise to blue emission [43,44].

The peak position of cyan luminescence is red-shifted with $Li_{0.5}Dy_{0.5}TiO_3$ doping and then got almost saturated with further doping as shown in **Figure 5.10 (c)**. We observed that $Li_{0.5}Dy_{0.5}TiO_3$ doping increase the PL intensity of cyan-emitting luminescence band as well as cause broadening of peak as shown in **Figure 5.10 (d)**. We found that after $Li_{0.5}Dy_{0.5}TiO_3$ doping $LiNbO_3$ shows a new yellow band energy position which blue shifted with increasing the doping concentration (see **Figure 5.10 (c)**). The intensity of yellow colour emission band increases with increasing concentrations of $Li_{0.5}Dy_{0.5}TiO_3$ from 0 .00625 to 0.125 in $LiNbO_3$ (see **Figure 5.10 (d)**). The source of yellow band could be dislocations, surface defects, oxygen vacancy or point defects[45]. The yellow emission band is generated by the recombination of donor-acceptor couples located within depletion zones that are linked to grain interfaces. This yellow band transition is due to donor-acceptor pair type transition [45]. Observation of yellow light emission in YAG:Dy^{3+} crystal is also reported[46]. The yellow light emission of Dy^{3+} originate during radiative transition of $4F_{9/2}$ levels on the lower energy levels ^6H_J (J = 9/2, 11/2. 13/2 & 15/2)[47]. From the **Figure 5.10(d)**, the PL intensity of yellow band increases from 393 to 1183 with increasing doping concentration to x = 0.025. The increase in intensity can be related to increase in number of donor-acceptor pairs with doping. When doping concentration further increased, there is a drop in intensity is observed which may be due to excess carriers recombination [45]. The variation in photoluminescence (PL) emission intensity is associated with the lithium-to-niobium (Li/Nb) ratio in ceramics. A noteworthy observation is that the intensity tends to rise as the Li/Nb ratio increases. Elevated concentrations of lithium ions (Li^+) prove advantageous for positioning electrons at energy levels, specifically at $^4F_{g/2}$, facilitating a beneficial impact on the radiative relaxation process[48]. The peak broadening of yellow band is maximum for x = 0.025 composition and this broadening is attributed to angular distribution of dipole moments which affected by doping higher concentration cause lowering of yellow band peak [45].

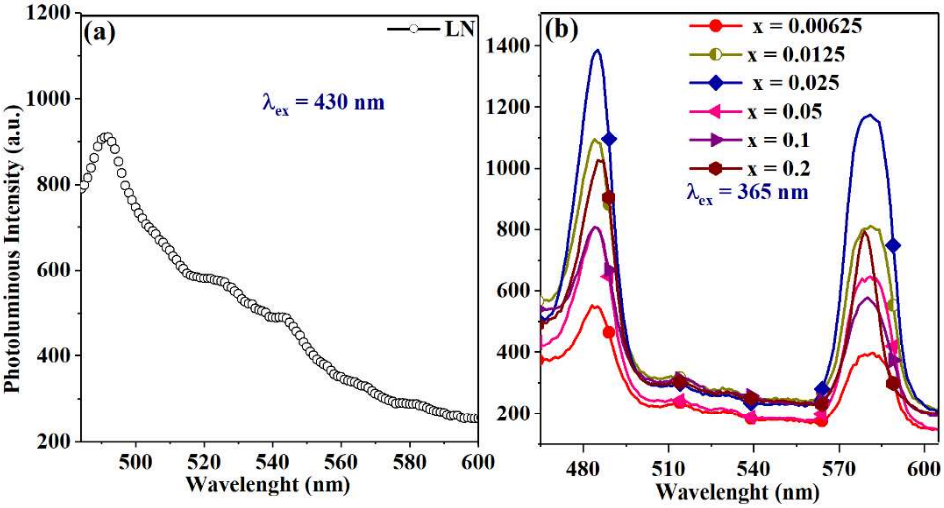

Figure 5.9 (a-b): (a) Photoluminescence spectra of $LiNbO_3$ solid solution (b) Photoluminescence spectra for $(1-x)LiNbO_3-xLi_{0.5}Dy_{0.5}TiO_3$ solid solutions with composition variation.

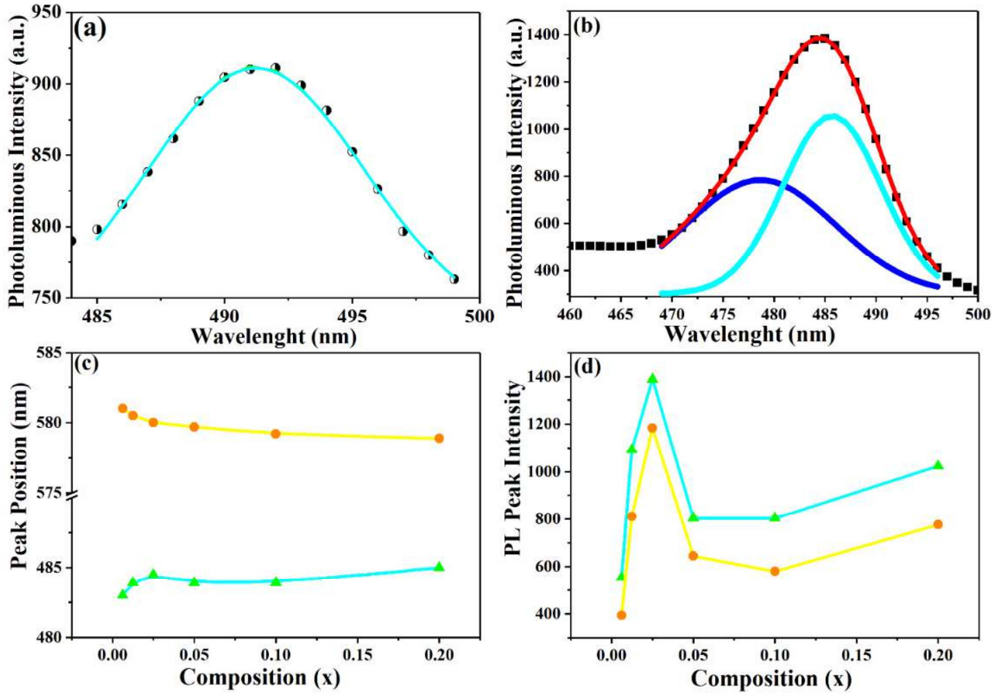

Figure 5.10(a-d): (a) Photoluminescence spectra of $LiNbO_3$ solid solution showing cyan colour emission spectrum peak fitting, (b) Photoluminescence spectra of $(1-x)LiNbO_3-xLi_{0.5}Dy_{0.5}TiO_3$ (x = 0.025) solid solution showing blue and cyan colour emission spectrum peak fitting, (c) Variation of peak position of cyan and yellow band with varying x in $(1-x)LiNbO_3-xLi_{0.5}Dy_{0.5}TiO_3$ solid solutions, (d) Variation of peak intensity of cyan and yellow band with varying x in $(1-x)LiNbO_3-xLi_{0.5}Dy_{0.5}TiO_3$ solid solutions.

5.3.8 Dielectric analysis

In **Figure 11(a-f)** we have shown the dielectric behavior of lithium niobate dysprosium titanate based solid solution ceramic materials at different constant frequencies (1 kHz in the **Figure 5.11(a),** 100 kHz in the **Figure 5.11**(c) and 1 MHz in the **Figure 5.11(e)**) with function of temperature with different compositions. From the shown figures, it is an interesting result arises as the doping concentration of dysprosium titanate in lithium niobate increases. The dielectric constant of this ceramic firstly enhanced till from the concentration of value x = 0.00625 to x = 0.05 as compared to prepared pure Lithium niobate ceramic. This may be happening due to variable oxidation state of Nb like +2, +3, +4 and +5 as Ti and Dy doping, Ti exist mostly in +4 oxidation state at some limitation, it is fixable in Nb place but after the concentration increases from x = 0.05 the dielectric constant decreases this may be due to the large difference in Ti and Dy compare to Li and Nb and mixed phase arises at that position which discussed in the crystal structure analysis part and XPS analysis part. At the lower frequencies material show high dielectric constant but when frequencies increase up to MHz its show low dielectric constant. This could be because at higher frequencies there is deficit of polarization, and the dielectric constant decreases at an increasingly rapid rate with the increase in frequency. The decrease is attributed to the diminished prominence of the space charge polarization effect. As a consequence of this, prepared ceramic shows a higher dielectric constant at low frequencies. The observed phenomenon may be attributed to space charge polarization occurring at the grain boundaries, leading to the formation of a potential barrier.

The dielectric loss is also shown for this ceramic at the same frequencies in the figures (at 1 kHz in the **Figure 5.11(b)**, at 100 kHz in the **Figure 5.11(d)** and at 1 MHz in the **Figure 5.11(f)**). The ratio of the imaginary part Ɛ" to the real part Ɛ' is the formula used to calculate the dielectric loss tangent, which is denoted by the symbol tan(δ), i.e. given by, tan(δ) = Ɛ"/ Ɛ'. This tangent relates to the phenomenon of dielectric relaxation, in which the loss of dielectric material indicates the amount of energy dissipated. This phenomenon arises when changes in polarization happen at the interfaces between grains in response to an externally applied electric field [49]. Dielectric loss in dielectric materials is caused by three primary factors: conduction of direct current (DC), migration of space charges resulting in interfacial polarization, and movement of molecular dipoles, referred to as dipole loss. In most of the cases, these three phenomena are responsible for the majority of the dielectric loss. It is observed that the tangent loss is independent up to 300 °C then rapid increase. It has also been found that the tangent loss is greater at lower frequencies, while at higher frequencies it is reduced to lesser values. This is something that was observed. The higher tanδ value obtained at lower frequencies is likely due to the increased resistivity of grain borders, which has a greater impact than the resistivity inside the grains themselves. This high resistivity makes grain boundaries responsible for the high value.

After reaching a certain temperature, there could be a second reason for the rapid increase in the value of the dielectric constant with increasing temperature. As the temperature rises, the thermal activation of the hopping of charge carriers occurs; consequently, An increase in dielectric polarization leads to a corresponding increase in the dielectric constant[50]. The maximum dielectric constant observed at composition x = 0.05 and calculated uniform grain size for this composition is smallest than others composition and it is found that 1.09 μm and The dielectric constant can also be significantly influenced by a variety of other important parameters, including the mobility of domain walls and the total number of domains. Uniform grain size enhances the ease and predictability of domain wall motion, resulting in an increase in the dielectric constant. During the Curie temperature, there is a phase transition that causes mechanical changes in the unit cells, resulting in the creation of internal stress within the material. Internal stress is influenced by both grain size and the uniformity of grain size. Greater uniformity in grain size leads to reduced internal stress, thereby promoting the motion of domain walls [50,51].

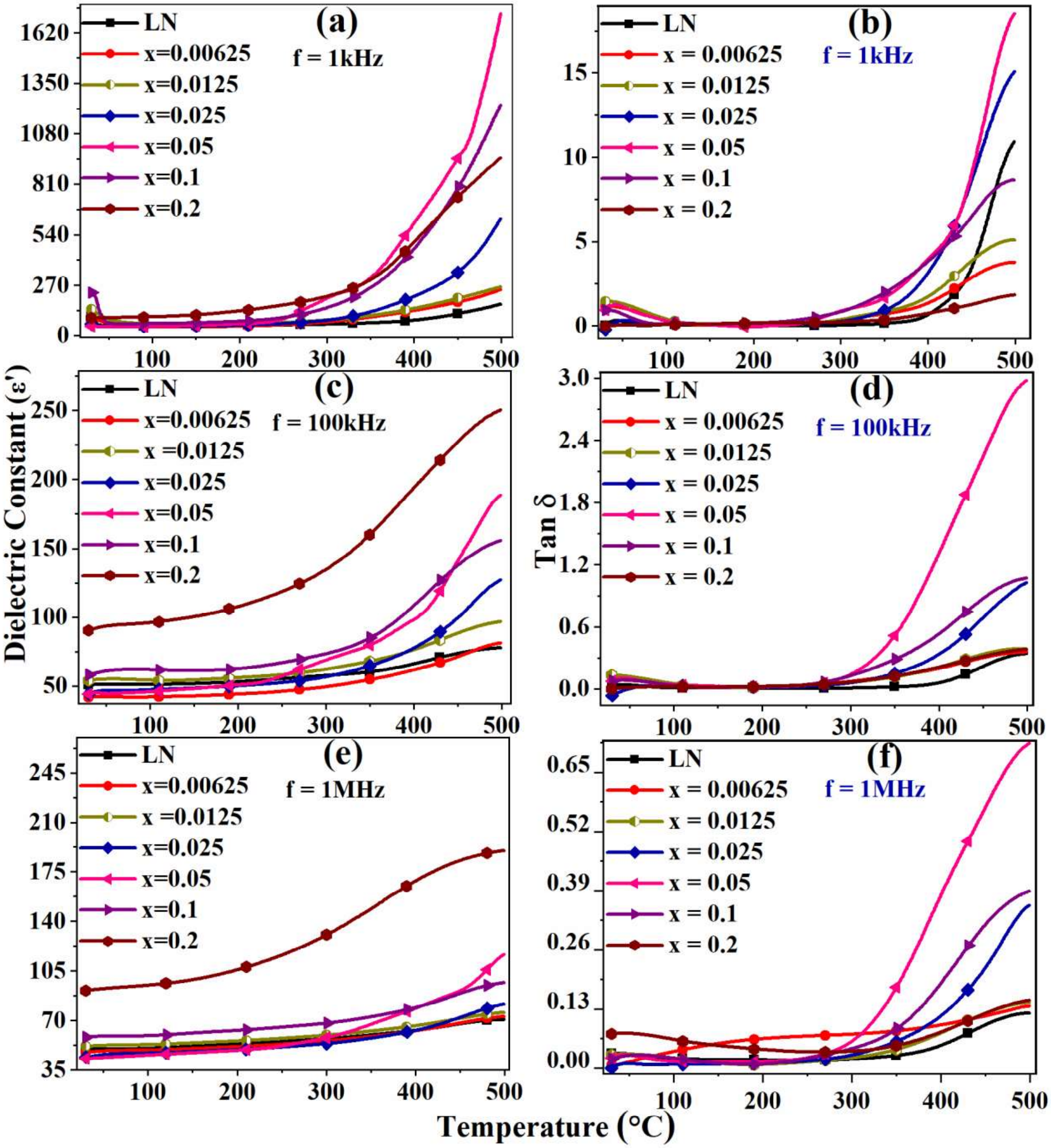

Figure 5.11 (a-f): Dielectrics behavior of (1-x)LiNbO$_3$+x(Li$_{0.5}$Dy$_{0.5}$)TiO$_3$ for different value of x (a) Permittivity at varying temperature at 1 kHz, (c) at 100 kHz (e) at 1MHz, Tangent loss at varying temperature at (b) 1 kHz, (d) 100 kHz and (f) 1MHz.

5.3.9 Polarization-Electric field analysis

The **Figure 5.12(a)** illustrates the hysteresis loop of polarization versus electric field (P-E) at room temperature, depicting various compositions. It is observed that the PE hysteresis loop changes with composition and it is found that the remnant polarization (P_r) is firstly decreases and then increases but the coercive field (E_C) firstly increases then decreases for the prepared lithium niobate dysprosium titanate based solid solutions.

It has been observed that in the case of pure lithium niobate and extremely low values of composition (denoted as x), the polarization-electric hysteresis curve exhibits a "non-ideal" behavior. This deviation is attributed to significant leakage, which is induced by the presence of oxygen vacancies, as reported by previous researchers. The existence of these vacancies is attributed to the diffusion of lithium and oxygen at the surface during the sintering process [52,53]. In this present work it is found that we have very much enhanced ferroelectric properties compared to some previous reported like, Mareno et al. reported the enhanced ferroelectric property of lanthanum doped Lithium Niobate and they found that the P_s is 0.235 μC/cm^2, P_r is 0.141 μC/cm^2 and Moreno et al. reported the ferroelectric properties of nano crystalline lithium niobate with P_s 0.21 μC/cm^2 and P_r 0.11 μC/cm^2 and one reported was reported by S. Banerjee and colleagues with P_r ~0.00026 μC/cm^2 for mesoporous lithium niobate[52,54,55]. Barik et al. also examined and reported the ferroelectric property of nano sized lithium niobate with P_s is 0.133 and P_r is 0.056 [56]. The ferroelectric properties of the pure $LiNbO_3$ are due to the crystal structural. The ferroelectric structure of $LiNbO_3$ is rhombohedral that belongs to the space group R3c having unit cell of 10 atoms. The oxygen atoms are stacked in such a way that their faces are aligned along the polar trigonal axis in the atomic arrangement. Along the axis of the trigonal pyramid, the transition metal atom has moved its position so that it is no longer at the middle of the oxygen octahedra. The subsequent oxygen octahedron along this axis does not contain any atoms, and the octahedron that is close to it contains an atom of lithium that has been ferro electrically displaced from the oxygen face in the direction of spontaneous polarization P_s.

Further, doping of the (Li, Dy)TiO_3 have the Ti and O. It is already known that Ti has 3d orbitals which lead to hybridization with oxygen p orbitals; this hybridization causes the tilt of octahedral causing the shift of the Ti from it center position. The shift of the Ti from the center position is responsible for the polarization. So, the enhancement in polarization to LNDT is due to the TiO_6 as the more amount of the LDT is added. The ferroelectric energy efficiency, defined by the ratio of the stored energy density to the overall energy density, demonstrates a strong relationship with variation of composition in this ceramic and this is potentially directing material design for various applications where capacitors uses with greater energy densities and reduced losses. Table 3 shows all of the characteristics linked to energy density characterizations for $(1-x)LiNbO_3+x(Li_{0.5}Dy_{0.5})TiO_3$ with various compositions.

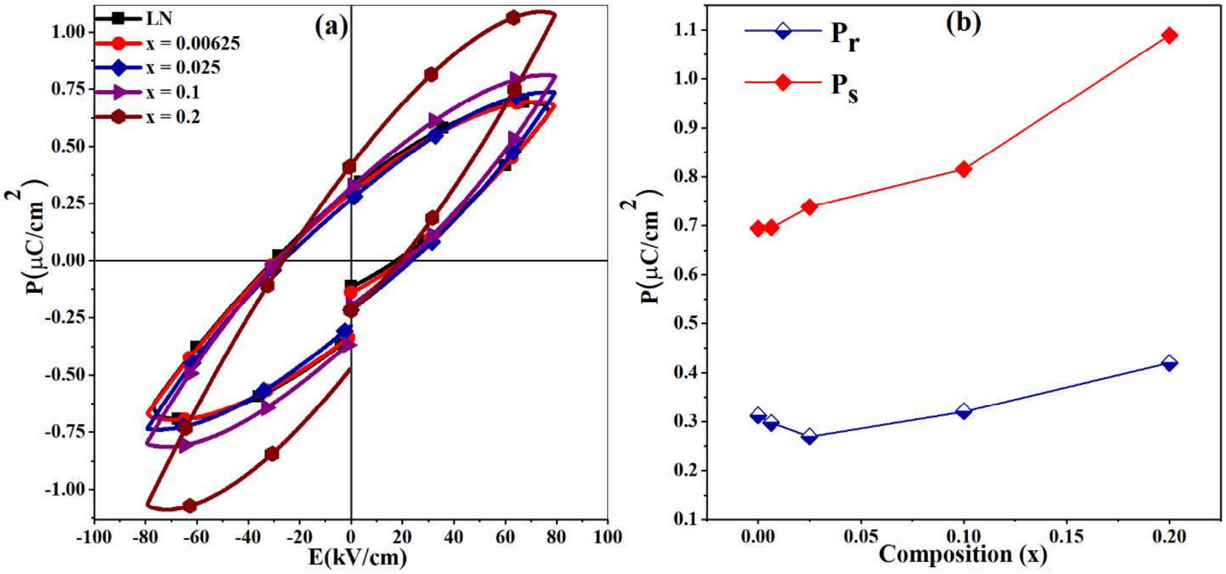

Figure 5.12(a-b): (a) Ferroelectric behavior and (b) Composition vs Polarization, of $(1-x)LiNbO_3-x(Li_{0.5}Dy_{0.5})TiO_3$

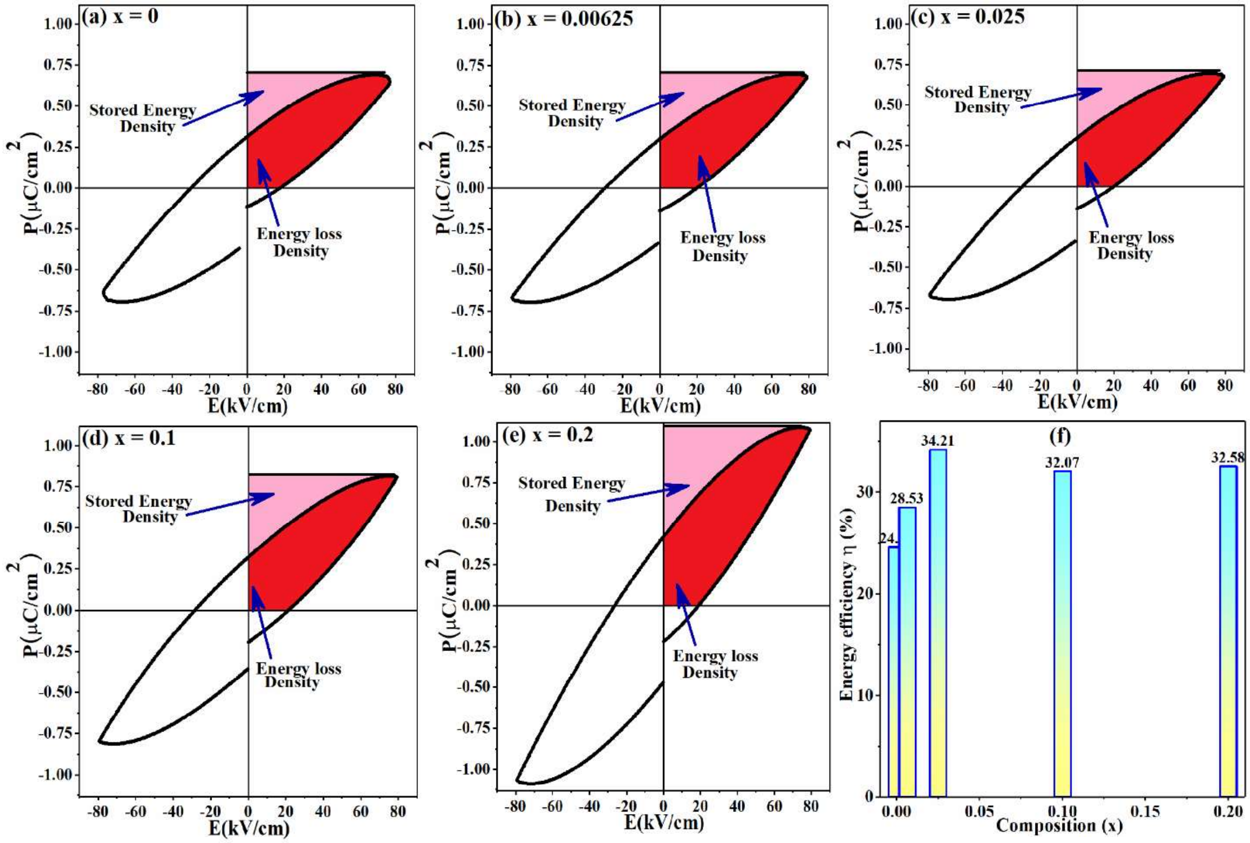

Figure 5.13(a-f): (a-e) P-E Energy hysteresis loop showing the are representing storage energy density and energy loss density and (f) Energy efficiency (%) with varying composition of (1-x)$LiNbO_3$-x$(Li_{0.5}Dy_{0.5})TiO_3$.

Table: 5.3. Electrical energy density and energy efficiency for (1-x)$LiNbO_3$-x$(Li_{0.5}Dy_{0.5})TiO_3$ with varying compositions

Composition	**Recoverable Energy density W_R (mJ/cm^3)**	**Total Energy density W_T (mJ/cm^3)**	**Energy loss density W_L (mJ/cm^3)**	**Energy efficiency (η) %**
x = 0	8.50	34.53	26.03	24.62
x = 0.00625	10.20	35.765	25.56	25.55
x = 0.025	13.68	39.87	26.19	34.00
x = 0.1	13.78	42.98	29.20	32.07
x = 0.2	17.96	55.11	37.15	32.58

5.4 Conclusions

Various compositions of (1-x)$LiNbO_3$-x$(Li_{0.5}Dy_{0.5})TiO_3$ solid solutions have been prepared by using high energy ball mill. Rietveld structure refinement for the prepared samples exhibits presence of two phases; one cubic phase and another hexagonal phase. Average grains size of (1-x)$LiNbO_3$-x$(Li_{0.5}Dy_{0.5})TiO_3$ solid solutions varies from 3.46 µm to 1.09 µm. The X-ray photoelectron spectroscopy analyses revealed the presence of oxygen vacancies as well as the different oxidation states of the constituent elements like O^{1-}, O^{2-}, Nb^{5+}, Dy^{3+}, Ti^{4+} and Ti^{3+}. The Thermogravimetric analysis revealed that the gain in weight with oxidation. Direct band gap first decreases with $(Li_{0.5}Dy_{0.5})TiO_3$ till x = 0.05 and start increasing after x = 0.05. The (1-x)$LiNbO_3$-x$(Li_{0.5}Dy_{0.5})TiO_3$ solid solutions with x > 0 emit blue, cyan and yellow colors. The yellow color emission was found to be most intense. The doped samples may be quite useful for the yellow laser applications. At room-temperature, ferroelectric response of the studied system increases with increasing doping concentration. Investigations of frequency and temperature dependent dielectric constant in the wide range of frequency from 1 kHz to 1 MHz and temperature from room-temperature to 500 °C reveal that both dielectric constant and dielectric loss decreased with increase in frequencies for all the compositions.

References:

[1] L.X. Lovisa, T.B.O. Nunes, E.C. Tavares, R.C.L. Machado, L.F. Dos Santos, M.R.D. Bomio, F. V. Motta, Effects of rare earth ions on structural, morphological and photoluminescent properties of non-stoichiometric $LiNbO_3$, Appl. Phys. A Mater. Sci. Process. 130 (2024). https://doi.org/10.1007/s00339-024-07399-6.

[2] Y. Saito, H. Takao, T. Tani, T. Nonoyama, K. Takatori, T. Homma, T. Nagaya, M. Nakamura, Lead-free piezoceramics, Nature. 432 (2004) 84–87.

[3] J. Li, Y. Li, Z. Zhou, R. Guo, A.S. Bhalla, Piezoelectric and ferroelectric properties of lead-free niobium-rich potassium lithium tantalate niobate single crystals, Mater. Res. Bull. 49 (2014) 206–209. https://doi.org/10.1016/j.materresbull.2013.08.077.

[4] S.K. Satyarthi, The Study of MgO Nano-Composite : Synthesis , Characterization and Probable Application submitted in partial fulfillment of the requirement,.

[5] D. Kumar, A.K. Singh, Investigation of structural and magnetic properties of $Nd_{0.7}Ba_{0.3}Mn_{1-x}Ti_xO_3$ (x = 0.05, 0.15 and 0.25) manganites synthesized through a single-step process, J. Magn. Magn. Mater. 469 (2019) 264–273.

[6] D. Kumar, C.B. Singh, N.K. Verma, A.K. Singh, Synthesis and structural investigations on multiferroic $Ba_{1-x}Sr_xMnO_3$ perovskite manganites, Ferroelectrics. 518 (2017).

[7] A. Tumuluri, K.C.J. Raju, Luminescence of $LiNbO_3$ polycrystalline ceramics: Effect of Sc_2O_3 and Lu_2O_3 doping, Ceram. Int. 40 (2014) 3371–3377.

[8] H. Kishi, N. Kohzu, J. Sugino, H. Ohsato, Y. Iguchi, T. Okuda, The effect of rare-earth (La, Sm, Dy, Ho and Er) and Mg on the microstructure in $BaTiO_3$, J. Eur. Ceram. Soc. 19 (1999) 1043–1046. https://doi.org/10.1016/s0955-2219(98)00370-7.

[9] J. Zhan, D. Liu, W. Du, Z. Wang, P. Wang, H. Cheng, B. Huang, M. Jiang, Synthesis and characterization of high crystallinity, well-defined morphology stoichiometric lithium niobate nanocrystalline, J. Cryst. Growth. 318 (2011) 1121–1124.

[10] V.P. Singh, C.B. Singh, S.K. Satyarthi, D. Kumar, A.K. Singh, Highly enhanced energy storage properties of H_2O_2-hydroxylated rare earth ferrites ($LaFeO_3$ and $GdFeO_3$) nanofillers in poly(vinylidene fluoride)-based nanocomposite films, J. Mater. Sci. Mater. Electron. (2022).

[11] V.P. Singh, S.K. Satyarthi, A. Dwivedi, A. Dwivedi, A.K. Singh, Boosting Energy Storage of Poly (vinylidene difluoride) Nanocomposite Based Flexible Self-Standing Film with Low Amount of Hydroxylated V_2O_5, (2022).

[12] H. Nakano, S. Suehiro, S. Furuya, K. Fukuda, Microstructural comparison between Nb- and Ta-systems in $Li1_{+x-y}M1_{-x-3y}Tix_{+4y}O_3$(M = Nb^{5+}, Ta^{5+}) solid solution with superstructure, J. Alloys Compd. 618 (2015) 504–507.

[13] R. Singh, S.B. Narang, phase solid solutions, 43 (2017) 10217–10223.

[14] D.K. Schreiber, R. Schwaiger, M. Heilmaier, S.J. McCormack, Materials properties characterization in the most extreme environments, MRS Bull. 47 (2022) 1128–1142.

[15] M.C. Maldonado-Orozco, M.T. Ochoa-Lara, J.E. Sosa-Márquez, S.F. Olive-Méndez, F. Espinosa-Magaña, Synthesis and characterization of electrospun $LiNbO_3$ nanofibers, Ceram. Int. 41 (2015) 14886–14889. https://doi.org/10.1016/j.ceramint.2015.08.013.

[16] K.C. Lo, Y.J. Chang, H. Murakami, J.W. Yeh, A.C. Yeh, An oxidation resistant refractory high entropy alloy protected by $CrTaO_4$ -based oxide, Sci. Rep. 9 (2019).

[17] X. Chen, T. Ma, X. Zhai, C. Lei, Thermogravimetric and infrared spectroscopic study of bituminous coal spontaneous combustion to analyze combustion reaction kinetics, Thermochim. Acta. 676 (2019) 84–93. https://doi.org/10.1016/j.tca.2019.04.002.

[18] L.Q. Wu, S.Q. Li, Y.C. Li, Z.Z. Li, G.D. Tang, W.H. Qi, L.C. Xue, L.L. Ding, X.S. Ge, Presence of monovalent oxygen anions in oxides demonstrated using X-ray

photoelectron spectra, Appl. Phys. Lett. 108 (2016).

[19] S. Li, D. Li, S. Li, G. Wang, X. Sun, L. Xu, H. Yuan, Local Structure and Room Ferromagnetism of Fe-Doped $LiNbO_3$ Films, J. Supercond. Nov. Magn. 35 (2022) 2897–2902. https://doi.org/10.1007/s10948-022-06341-2.

[20] P. Gu, X. Zhu, H. Wu, J. Li, D. Yang, Influence of oxygen vacancy on the response properties of TiO_2 ultraviolet detectors, J. Alloys Compd. 779 (2019) 821–830.

[21] E.A. Skryleva, I. V. Kubasov, P. V. Kiryukhantsev-Korneev, B.R. Senatulin, R.N. Zhukov, K. V. Zakutailov, M.D. Malinkovich, Y.N. Parkhomenko, XPS study of Li/Nb ratio in $LiNbO_3$ crystals. Effect of polarity and mechanical processing on $LiNbO_3$ surface chemical composition, Appl. Surf. Sci. 389 (2016) 387–394.

[22] A. Aribia, J. Sastre, X. Chen, E. Gilshtein, M.H. Futscher, A.N. Tiwari, Y.E. Romanyuk, In Situ Lithiated ALD Niobium Oxide for Improved Long Term Cycling of Layered Oxide Cathodes: A Thin-Film Model Study, J. Electrochem. Soc. 168 (2021) 040513. https://doi.org/10.1149/1945-7111/abf215.

[23] Z. Vakulov, E. Zamburg, D. Khakhulin, A. Geldash, D.A. Golosov, S.M. Zavadski, A. V. Miakonkikh, K. V. Rudenko, A.P. Dostanko, Z. He, O.A. Ageev, Oxygen pressure influence on properties of nanocrystalline linbo3 films grown by laser ablation, Nanomaterials. 10 (2020) 1–13. https://doi.org/10.3390/nano10071371.

[24] W.H. Lee, J.U. Woo, H.G. Hwang, S. Nahm, G.B. Lee, J.W. Choi, $Sr_2Nb_3O_{10}$ nanosheet thin film grown via LB method for high-performance planar-type pseudocapacitor, Appl. Surf. Sci. 525 (2020) 146640.

[25] Z.L. Tseng, L.C. Chen, J.F. Tang, M.F. Shih, S.Y. Chu, Thickness Effect of Nb-Doped TiO_2 Transparent Conductive Oxide Grown on Glass Substrates Fabricated by RF Sputtering, J. Electron. Mater. 46 (2017) 1476–1480.

[26] J. Wu, J. Li, J. Liu, J. Bai, L. Yang, A novel Nb_2O_5/Bi_2WO_6 heterojunction photocatalytic oxidative desulfurization catalyst with high visible light-induced photocatalytic activity, RSC Adv. 7 (2017) 51046–51054.

[27] D. Recktenwald, C.C. Mardare, A.I. Mardare, L.I. Jinga, G. Socol, A.W. Hassel, Combinatorial screening of dysprosium-magnesium-zinc alloys for bioresorptive implants, Electrochim. Acta. 363 (2020) 137106.

[28] D. Wang, G. He, L. Hao, J. Gao, M. Zhang, Comparative passivation effect of ALD-driven HfO_2 and Al_2O_3 buffer layers on the interface chemistry and electrical characteristics of Dy-based gate dielectrics, J. Mater. Chem. C. 7 (2019) 1955–1965.

[29] K.W. Sung, D.Y. Shin, H.J. Ahn, Boosting ultrafast Li storage kinetics of conductive Nb-doped TiO_2 functional layer coated on $LiMn_2O_4$, J. Alloys Compd. 870 (2021) 159404. https://doi.org/10.1016/j.jallcom.2021.159404.

[30] B. Zhong, Z. Long, C. Yang, Y. Li, X. Wei, Colossal dielectric permittivity in co-doping $SrTiO_3$ ceramics by Nb and Mg, Ceram. Int. 46 (2020) 20565–20569.

[31] L. Kovács, M. Wohlecke, A. Jovanović, K. Polgár, S. Kapphan, Infrared absorption

study of the OH vibrational band in $LiNbO_3$ crystals, J. Phys. Chem. Solids. 52 (1991) 797–803. https://doi.org/10.1016/0022-3697(91)90078-E.

[32] R.K. Choubey, B.Q. Khattak, S. Kar, P. Ramshankar, P. Sen, K.S. Bartwal, Influence of doping on OH absorption in $LiNbO_3$ crystals, Cryst. Res. Technol. 42 (2007).

[33] G. Bhagavannarayana, R. V. Ananthamurthy, G.C. Budakoti, B. Kumar, K.S. Bartwal, A study of the effect of annealing on Fe-doped $LiNbO_3$ by HRXRD, XRT and FTIR, J. Appl. Crystallogr. 38 (2005) 768–771. https://doi.org/10.1107/S0021889805023745.

[34] C. An, K. Tang, C. Wang, G. Shen, Y. Jin, Y. Qian, Characterization of $LiNbO_3$ nanocrystals prepared via a convenient hydrothermal route, Mater. Res.Bull. 37 (2002).

[35] J. Tauc, Optical properties and electronic structure of amorphous Ge and Si, Mater. Res. Bull. 3 (1968) 37–46. https://doi.org/10.1016/0025-5408(68)90023-8.

[36] S. Çabuk, A. Mamedov, Urbach rule and optical properties of the $LiNbO_3$ and $LiTaO_3$, J. Opt. A Pure Appl. Opt. 1 (1999) 424–427.

[37] C.B. Singh, D. Kumar, N.K. Verma, A.K. Singh, Structural, dielectric, semiconducting and optical properties of high-energy ball milled $YFeO_3$ nano-particles, AIP Conf. Proc. 2115 (2019) 8–12. https://doi.org/10.1063/1.5113458.

[38] L. Mühlenbein, C.B. Singh, A.K. Singh, I. Fina, C. Himcinschi, A. Lotnyk, A. Bhatnagar, Control of Layering in Aurivillius Phase Nanocomposite Thin Films and Influence on Ferromagnetism and Optical Absorption, ACS Appl. Electron. Mater. 4 (2022) 1997–2004. https://doi.org/10.1021/acsaelm.2c00160.

[39] C. Bhal Singh, N. Kumar Verma, A. Kumar Singh, Synthesis and band-gap tuning of (Co, Bi) doped $PbTiO_3$ for photoferroelectrics applications, Integr. Ferroelectr. 194 (2018) 145–151. https://doi.org/10.1080/10584587.2018.1514886.

[40] L. Tang, white light-emitting diodes, 11 (2013) 4–7.

[41] Z.H. Tang, S.P. Lin, D.C. Ma, B. Wang, Blue and green upconversion emissions of Zr:Nd:$LiNbO_3$ single crystals, Int. J. Mod. Phys. B. 29 (2015) 1–11.

[42] M. Malinowski, P. Myziak, R. Piramidowicz, I. Pracka, T. Łukasiewicz, B. Surma, S. Kaczmarek, K. Kopczyński, Z. Mierczyk, Spectroscopic and Laser Properties of $LiNbO_3$:Dy^{3+} Crystals, Acta Phys. Pol. A. 90 (1996) 181–189.

[43] Z. Min, Q. Zeng, S. Chen, Y. Qin, C. Yao, Tunable photoluminescence of $LiNbO^3$: RE^{3+} (RE^{3+} = Dy^{3+}, Sm^{3+}, Dy^{3+}/Sm^{3+}) single-phase phosphors for warm white LEDs, J. Alloys Compd. 924 (2022) 166497. https://doi.org/10.1016/j.jallcom.2022.166497.

[44] G. Dominiak-Dzik, W. Ryba-Romanowski, M.N. Palatnikov, N. V. Sidorov, V.T. Kalinnikov, Dysprosium-doped $LiNbO_3$ crystal. Optical properties and effect of temperature on fluorescence dynamics, J. Mol. Struct. 704 (2004) 139–144. https://doi.org/10.1016/j.molstruc.2004.01.063.

[45] M. Matys, B. Adamowicz, Mechanism of yellow luminescence in GaN at room temperature, J. Appl. Phys. 121 (2017). https://doi.org/10.1063/1.4975116.

[46] R. Lisiecki, B. Macalik, R. Kowalski, J. Komar, W. Ryba-Romanowski, Effect of temperature on luminescence of $LiNbO_3$ crystals single-doped with Sm^{3+}, Tb^{3+}, or Dy^{3+} ions, Crystals. 10 (2020) 1–15. https://doi.org/10.3390/cryst10111034.

[47] S.R. Bowman, S. O'Connor, N.J. Condon, Diode pumped yellow dysprosium lasers, Opt. Express. 20 (2012) 12906. https://doi.org/10.1364/oe.20.012906.

[48] Y. Furukawa, M. Sato, K. Kitamura, Y. Yajima, M. Minakata, Optical damage resistance and crystal quality of $LiNbO_3$ single crystals with various [Li]/[Nb] ratios, J. Appl. Phys. 72 (1992) 3250–3254. https://doi.org/10.1063/1.351444.

[49] C. Rayssi, S. El Kossi, J. Dhahri, K. Khirouni, Frequency and temperature-dependence of dielectric permittivity and electric modulus studies of the solid solution $Ca_{0.85}Er_{0.1}Ti_{1-:x}CO_{4}$ x $_{/3}O_{3}$ ($0 \leq x \leq 0.1$), RSC Adv. 8 (2018) 17139–17150.

[50] V.R. Mudinepalli, L. Feng, W.C. Lin, B.S. Murty, Effect of grain size on dielectric and ferroelectric properties of nanostructured $Ba_{0.8}Sr_{0.2}TiO_3$ ceramics, J. Adv. Ceram. 4 (2015) 46–53. https://doi.org/10.1007/s40145-015-0130-8.

[51] T.M. Shaw, S. Trolier-McKinstry, P.C. McIntyre, The Properties of Ferroelectric Films at Small Dimensions, Annu. Rev. Mater. Sci. 30 (2000) 263–298. https://doi.org/10.1146/annurev.matsci.30.1.263.

[52] C. Díaz-Moreno, R. Farias, A. Hurtado-Macias, J. Elizalde-Galindo, J. Hernandez-Paz, Multiferroic response of nanocrystalline lithium niobate, J. Appl. Phys. 111 (2012).

[53] C.A. Diaz-Moreno, R. Farias-Mancilla, J.T. Elizalde-Galindo, J. González-Hernández, A. Hurtado-Macias, D. Bahena, M. José-Yacamán, M. Ramos, Structural aspects $LiNbO_3$ nanoparticles and their ferromagnetic properties, Materials (Basel). 7 (2014).

[54] C.A. Diaz-Moreno, Y. Ding, J. Portelles, J. Heiras, A.H. Macias, A. Syeed, A. Paez, C. Li, J. López, R. Wicker, Optical properties of ferroelectric lanthanum lithium niobate, Ceram. Int. 44 (2018) 4727–4733. https://doi.org/10.1016/j.ceramint.2017.12.055.

[55] S. Banerjee, M. Kumar Bhunia, A. Bhaumik, D. Chakravorty, Multifunctional behaviour of mesoporous $LiNbO_3$, J. Appl. Phys. 111 (2012) 054310..

[56] R. Barik, S.K. Satpathy, B. Behera, S.K. Biswal, R.K. Mohapatra, Synthesis and Spectral Characterizations of Nano-Sized Lithium Niobate ($LiNbO_3$) Ceramic , Micro Nanosyst. 12 (2019) 81–86. https://doi.org/10.2174/1876402911666190617114003.